Fermi National
Accelerator Laboratory

Summer internship

Final report

Test of new sensors for the HL-LHC CMS upgrade

Author:
Andrea Lampis

Supervisor:
Petra Merkel
Ron Lipton

November 15, 2018

Abstract

The HL-LHC upgrade is expected to increase the instantaneous luminosity of the LHC by a factor of about five. Under these condition the performance degradation of detectors due to integrated radiation dose requires to all main CERN experiments to be upgraded. The CMS detector has to replace a big part of the tracker and the calorimeter. The new Calorimeter has the name of High Granularity Calorimeter and it will be realized as a sampling calorimeter, including 40 layers of silicon detectors. The sensors will be realized as pad detectors with an active thickness between 100 μm and 300 μm, and they will be provided by different companies. In this work I expose the studies, I have done during my internship, of the charge collection efficiency and leakage current for sensors produced by Nhanced Semiconductor.

1 Introduction

In this section are briefly introduced the LHC *Large Hadron Collider* particle accelerator and the CMS detector. It is also presented a summary of the upgrade of the CMS detector for the High Lumuinosity LHC upgrade.

1.1 LHC *Large Hadron Collider*

The Large Hadron Collider (LHC), shown in Figure 1, is the world largest and most powerful particle accelerator of the world. It is also the most powerful proton-proton collider ever built and it has been built at CERN in the same tunnel where the LEP (Large Electron-Positron Collider) was installed. The tunnel is 27 km long and is situated 100 m underground the Franco-Swiss border near Geneva.

Two transfer tunnels, each approximately 2.5 km in length, link the LHC to the CERN accelerator complex that acts as injector. In fact LHC relies on a chain of several particle accelerators, from the protons source to the final step (accelerated proton beams), several accelerator are used to accelerate and inject proton bunches into LHC machine. The protons originate in a 92 keV duoplasmatron source, fed with H_2 gas, yielding a 300 mA beam current. The protons from this source are collected as an input to LINAC2, which increases their energy up to 50 MeV. This LINAC supplies the PSB with protons for an increase in energy up to 1.4 GeV. All protons

Figure 1: Picture of LHC with main experiments.

are then accelerated by the PS, up to $25\,GeV$ and subsequently by the SPS, up to $450\,GeV$. The final step of beams acceleration takes place in LHC. It consists of two circulating beams in separate vacuum chambers which are horizontally spaced by $194\,mm$. Only at about $100\,m$ before the interaction point, the two beam pipes join into a single piece. Thanks to eight resonant cavities, these two pulsed beams are accelerated up to $7\,TeV$. The beams are steered by 1232 cryogenic dipole magnets with a field of $8\,T$, these dipoles are immersed in a pressurized bath of super-fluid Helium at $1.9\,K$ to maintain a superconducting state, storing an energy of about $600\,MJ$, the track of the accelerated beams is shown in Figure 2.

The beams inside the LHC are made to collide at four different locations around the ring were are located four big particle detectors: ATLAS, CMS, ALICE and LHCb. Each beam has 2808 circulating proton bunches, which are arranged in groups of 3 and 4 trains of 72 bunches, with 25 ns spacing within the train corresponding to 8 empty bunches between two trains. At every bunch crossing occur the collisions between the beams so the resulting maximum collisions rate is 40 MHz. In particle physics instead of the number of collisions we use the instantaneous luminosity $\mathscr{L}(t)$ which relates the cross section of a given process with the number of the expected events per unit of time in the collisions. Another important and related quantity is the integrated luminosity which is the time integral of the instantaneous luminosity, it permits to calculate the number of events of a process simply multiplying it by the cross section for that event. The current integrated luminosity at LHC is $68\,fb^{-1}$.

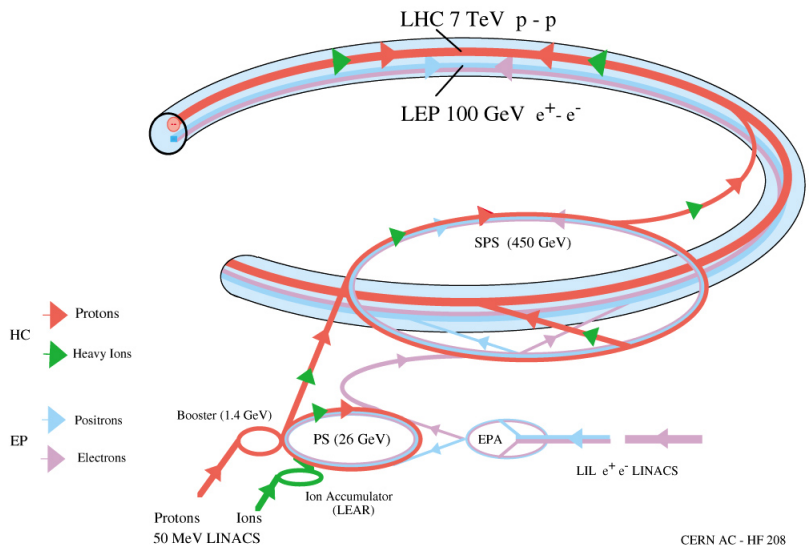

Figure 2: LHC injection complex.

1.2 CMS Detector

The Compact Muon Solenoid (CMS) experiment is a general-purpose particle detector, in fact its main goal is to explore physics at the TeV energy scale from the Standard Model measurements, including the Higgs boson and its properties, high precision tests of QCD, flavour physics and electroweak interaction, to the search for new physics beyond the Standard Model. CMS has a several cylindrical layers coaxial to the beam direction, called the barrel, closed at both ends by disk which are orthogonal to the beam pipe, called the endcaps.

The central part of the detector is a 13 m long superconducting solenoid with a diameter of 6 m, providing a 4 T axial magnetic field. As shown in Figure 3 CMS has a complex system of sub-detectors that allows to identify different particles with an high momentum resolution on a wide energy and angular coverage. The sub-detector system, starting from the interaction point and going outwards is composed by: the inner tracking system, the electromagnetic calorimeter, the hadron calorimeter, the magnet and the muon chambers.

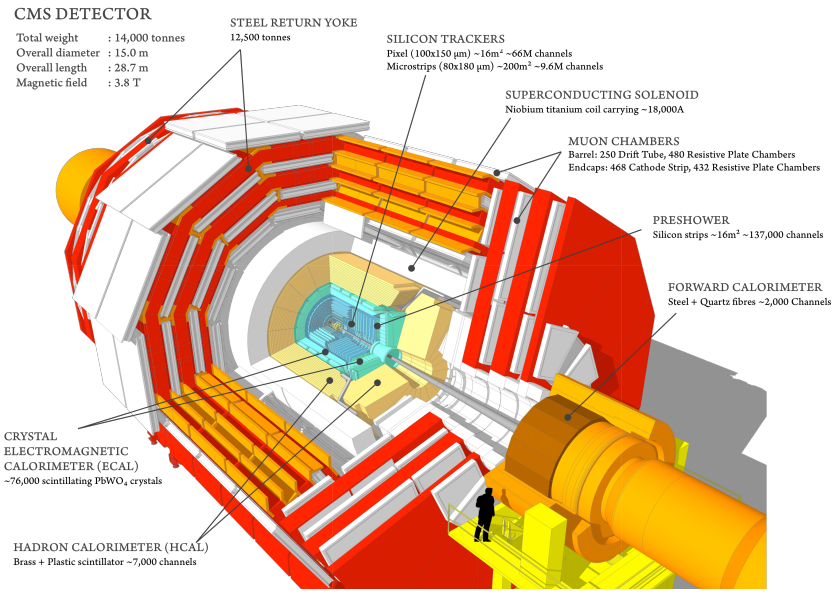

Figure 3: The CMS detector.

1.2.1 The tracking system

The main performances requirements for the tracker are a robust tracking and a detailed vertex reconstruction within a strong magnetic field. The tracker system must also be sufficiently radiation hard in order to guarantee his operation for the all period of data taking of the experiment. Due to its high segmentation the tracker produces high quality data for the offline track reconstruction algorithm and manages to identify unambiguously tracks coming from multiple vertex, but it is also used online in order to perform fast tracking in the high level trigger for primary vertex reconstruction, electron/photon identification, muon reconstruction, tau identification and b-tagging. The CMS tracker has a radius of 1.25 m and a length of 5.8 m and its acceptance $|\eta|$ is minor than 2.5. It is composed by two main sub-detectors, the first is the Pixel vertex detector system which is used for accurate measurement of the vertex position, and the second is the Silicon Strip which is used for accurate track reconstruction.

1.2.2 The Electromagnetic Calorimeter

The Electromagnetic Calorimeter (ECAL) is an hermetic and homogeneous calorimeter made up of 75848 scintillating crystals of Lead tungstate ($PbWO_4$). The choice of such material allows to ultimately achieve high granularity, fast radiation, radiation hardness and a very compact system. The crystals are arranged in three different dispositions, there is a barrel section, forming the ECAL barrel, and two endcaps , the ECAL EndCaps. The barrel covers a range $|\eta| < 1.479$ and the endcaps $1.479 < |\eta| < 3$. The light produced from the crystals is collected by photodetectors in order to be converted to an electrical signal and then amplified. The ECAL contains also a Preshower detector instrumented in front of the endcaps which allows to increase precision in the position determination, so to distinguish between single high-energy photons and close pairs of low-energy photons and therefore to prevent false signals.

1.2.3 The Hadron Calorimeter

The Hadron Calorimeter (HCAL) is an hermetic sampling calorimeter that allows to determine a particle's energy, position and arrival time. The HCAL is made up of alternating layers of active material and of absorber. The absorber, because it is inserted into a magnetic field, it has to be made of a non magnetical material, in fact it is made of cartridge brass (C26000), composed by 70% Cu and 30% by Zn. The active material is fluorescent scintillator. The light produced in the scinitillator is collected to hybrid photodiodes by waveleght-shifting fibers. The HCAL is organised into Hadron Calorimeter Barrel (HB), Endcap (HE) and Forward (HF) sections. The HB and HE regions are located around the ECAL. The HB covers the region $|\eta| < 1.3$ and is divided into two half barrel section. The Hadron Calorimeter Endcaps cover the range $1.3 < |\eta| < 3$. The HF is located 11.2 m away from the interaction point, allowing to include the range $3 < |\eta| < 5.2$ and is made up of quartz fibers embedded within a 165 cm long steel absorber. Additional scintillators compose the Hadron Calorimeter Outer(HO), and are placed outside the solenoid to ensure adequate sampling depth and to measure late shower development.

1.2.4 The Superconducting Magnet

Both the tracker and the two calorimeters are within a 4 T magnetic field which is generated by a superconducting solenoidal magnet coaxial to the beam. This magnet represent the central feature of the CMS design, its main task is to bend the paths of particles emerging from LHC high energy collisions. This high magnetic field combined with the high precision measurements made in the tracker and in muon detectors allows to the CMS detector to accurately measure also the momentum of high energy particle. The magnet system consists of a superconducting coil housed in a vacuum tank and of a return yoke. The iron return yoke has a 12-sided cylindrical structure. The central part is divided in 5 coaxial rings, each one consisting of three layers where the muon chambers are hosted, the endcaps yokes instead are made of three disks divided into 12 sectors. The superconducting coil is cooled down by liquid helium.

1.2.5 The muon system

As suggested from the name of the detector the muon detection is one of CMS's main design goals. Muons are important in order to reconstruct the events because they are products of many physics processes and because it is easy to identify them.The Muon System provides muon identification, triggering, and momentum reconstruction, and is located in the region outside the magnet. This is because the muons can penetrate several meters without interacting with the matter in the calorimeters and in the tracker, and so they are the only particles that can be revealed in the outher region. Moreover in this region, the presence of the return yoke allows the presence of a magnetic field of 1.8 T in the opposite direction with respect to the one inside the magnet. In this way, by collecting hits in the muon system, it is possible to reconstruct the muon track also adding the information coming from the tracker system. The Muon system is build by different type of particle detectors that allows to make the particle identfication (PID) and measure their momenta. There are 250 Drift Tubes (DT), 549 Cathode Strip Chambers (CSC) and 610 Resistive Plate Chambers (RPC). The DTs and the CSCs provide an excellent spatial resolution while the RPCs have a very good time resolution.

1.3 HL-LHC CMS Upgrade

The LHC accelerator after the so called Phase 2 upgrade will reach an instantaneous luminosity of $5 \cdot 10^{34} cm^{-2} s^{-1}$. This new projection for the instantaneous luminosity sets the particle occupancies, trigger requirements, and data rates that the experiments must be prepared to handle to fully exploit the potential of the accelerator. Also in this new condition an integrated luminosity of 4000 fb^{-1} could be delivered by the end of Phase II, this of course defines the new basic requirements for the detectors in terms of radiation hardness. So the main challenges that must be overcome in this upgrade are the radiation damage to the CMS detector from the large integrated luminosity and the huge pileup that comes from the high instantaneous luminosity. Simulations of the radiation damage with the data collected during the current run have been performed at the HL-LHC doses. The result from these studies tells that the tracker and the endcap calorimeters must be entirely replaced. With the replacement of these detectors also the performance issues associated with high pileup can be solved. Pileup can be observed in a single bunch-crossing by the many collision vertices that are reconstructed by the tracking system. The new tracking system can be designed with enough segmentation to associate charged particles with the correct interaction vertices. The present calorimeters in CMS however do not have capability to directly associate showers with particular vertices. This is likely to be possible with the new endcap calorimeters in which accurate timing, and finer lateral and longitudinal segmentation will be present. This can further improve pileup mitigation, particularly for neutral particles. The other sub-detector will not be replaced but most of the front end electronics will not survive on a such high radiation environment so it will be replaced.

1.3.1 Tracker system

To ensure adequate track reconstruction performance at the much higher pileup levels of the HL-LHC, a new tracker system is required. This new system must have an outer tracker with a granularity increased by a factor of 4 and a pixel detector with an increasing of granularity by a factor 6. With these new granularities the level of occupancies are similar to the actual state at a luminosity of $10^{34}\, cm^{-2} s^{-1}$. For the outher tracker the increasing in luminosity is achieved by new silicon sensors with shorter strips but without changing the pitch significantly.In the optimization process, the minimization

of the material in the tracker has been a major goal. Thanks to configuration improvements, special module design, and new techniques developed for the cooling and power distribution systems, the mass in the tracking volume is greatly reduced. Finally to reach the high radiation tolerance required, the sensors will be thinner and produced in the planar n-in-p technology.

1.3.2 High Granularity Calorimeter

The endcap calorimeters will be replaced by the new High Granularity Calorimeter (HGCAL). It has electromagnetic and hadronic sections with a very good transverse and longitudinal segmentation for 3D measurement of shower topologies. The elecromagnetic section (CE-E) consists of 28 tungsten and copper plates interleaved with silicon sensors. While the hadronic part (CE-H) consists of 12 brass and copper plates interleaved with silicon sensors, in the outermost region are used tiles of plastic scintillator. The design of this new detector, shown in Figure 4, will allow precise timing measurements, that permits to reduce pileup. The silicon sensor technology is n-in-p technology with three different active thickness depending on radiation doses. Each sensor has an hexagonal shape with a cross section of about 0.5 or 1 cm^2 depending on its thickness. Each hexagonal sensor is located in a hexagonal Wafer.

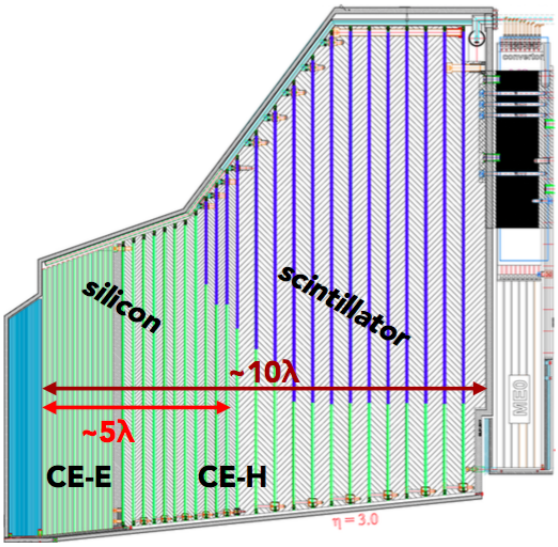

Figure 4: Scheme of the HGCAL.

All the module as shown in Figure 5 is built as a glued stack of Cu/W baseplate, the Silicon sensor it is directly connected with an adhesive layer to the printed circuit board which contains the readout chips. The Cu/W baseplate provides mechanical rigidity as well as a thermal pathway to the copper plate. The Cu/W baseplate provides mechanical rigidity as well as a thermal pathway to the copper plate. The copper plate contributes as absorber material, it provides mechanical support to the structure and hosts the cooling pipes for removal of heat from the sensor and from the readout electronics, maintaining the detector at -30 ° to limit the leakage current due to radiation.

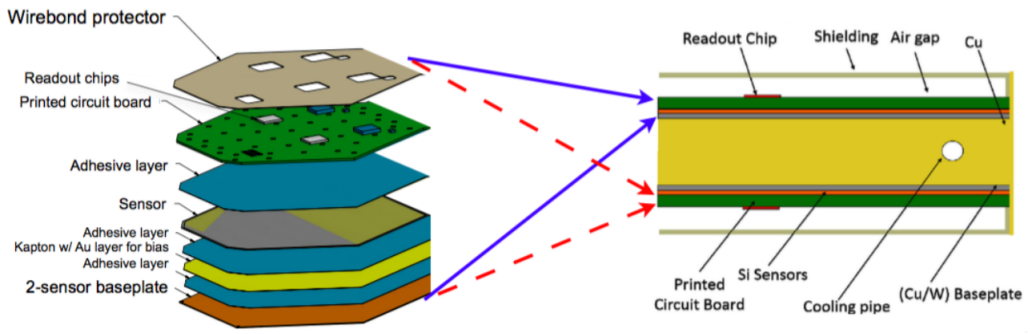

Figure 5: Scheme of a complete module of the HGCAL.

2 Tests for the detector prototypes

During my work I studied and tested 4 different prototypes of the silicon wafers for the HGCAL. The prototypes were all half size wafer with 200 μm thick produced by *Nhanced Semiconductor*. The only difference in this prototypes is a different concentration of p-dopant for the p-stops, that is a system that permits to isolate the channel from each other. In Figure 6 is shown an image of a prototype.

The test I made are:

- Laser test: I measured the signal height that comes from the detector when the light of a laser is focused on it. This measurement allows to study the charge collection efficiency of the detector as a function of the bias potential;

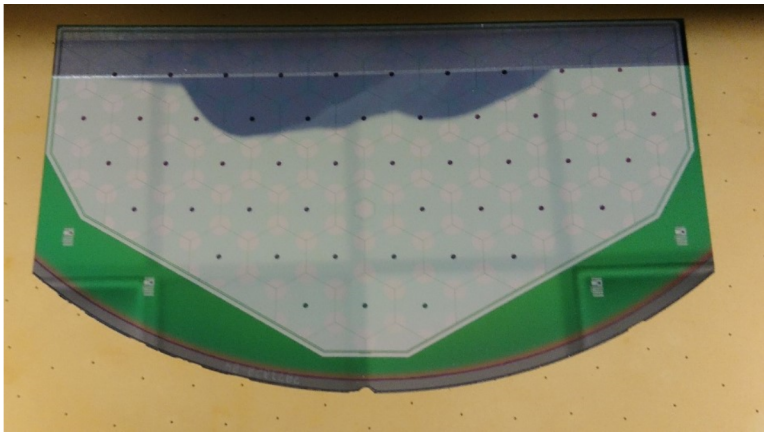

Figure 6: Half size Wafer prototype sensor for the HGCAL produced by Nhanced Semiconductor.

- VI study: I measured the leakage current as a function of the bias potential. This test allows to study the general behaviour of the detector;
- V study: in which I measure the potential of a single channel as a function of the bias potential. This study permits to have a rough knowledge of the isolation between channels.

All these tests are done with an automatic probe station, shown in Figure 7 which allows to perform systematic measurements for different channels of a silicon sensor. All of these tests are done for Nhanced prototypes half Wafers 1, 2, 3 and 4.

3 Laser Test

The laser test has the aim to measure the charge collection efficiency of each channel of the detector, in a more specific view the test I made were focused on the uniformity of the charge collection efficiency among the channels of the detector. All the channels of the wafer are tested except for the channels on the edges, because we noticed a strange behaviour of the electric field on the edges of the wafer, and the central channel, which is a calibration channel with a different geometry that required a different setup to be tested. The measurements for all the channels of a wafer are automatized by a LabVIEW

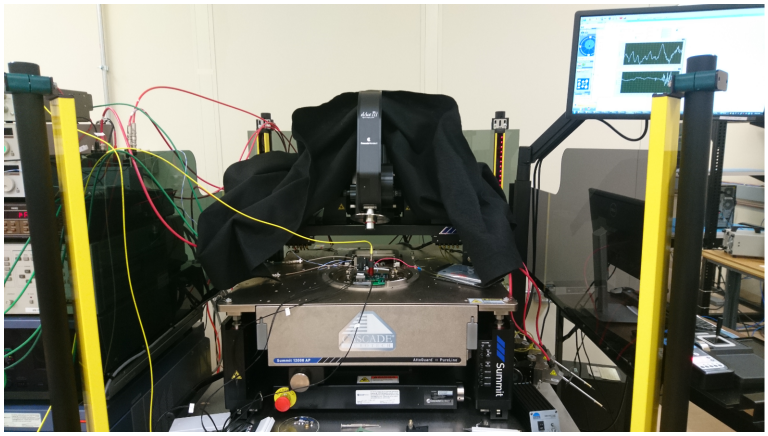

Figure 7: Automaric probe station Cascade Microtech Summit 12000 AP

software which controls all the instruments of the setup and it also acquires the data.

3.1 Setup

In figure 8 is shown a synthetic scheme of the setup used for the laser test. All the instruments in the setup are controlled by a LabView software which also permits to acquire the data.

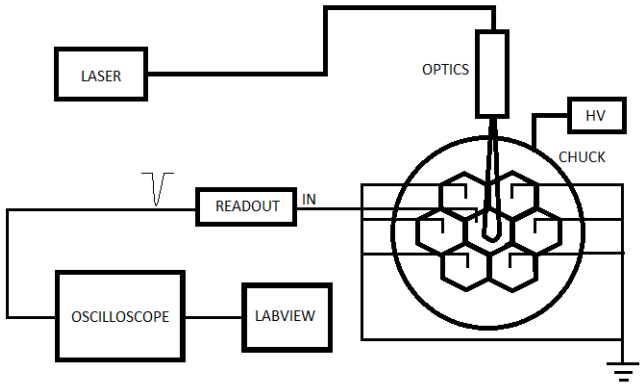

Figure 8: Scheme of the setup used for the laser test.

Figure 9: Laser used for the Laser test.

3.1.1 Laser

The Laser, shown in Figure 9 is used to simulate the passage of a MIP trough the detector in order to measure the charge collected in the detector. Its features are listed below:

- Wavelenght: $1053\,nm$;
- Pulse width: $50\,ps$.

The laser is triggered by a controller which emits a trigger for the laser with a frequency of $10\,kHz$. The laser signal is moved to the optics trough an optical fiber. The optics allows the detector to be irradiated.

3.1.2 Probe station

The probe station, shown in Figure 10 permits to make the systematic measurements for all the channels of a wafer. It has a chuck which is used to fix the sample with a vacuum system and it also make the contact to provide to all the channels on a wafer the bias potential. Is is controlled by a LabVIEW software that permits to move the chuck, in order to change the irradiated channel, and also the channel read via the readout card. When a new Wafer is inserted the operator has to made a manually calibration of the position frame of reference.

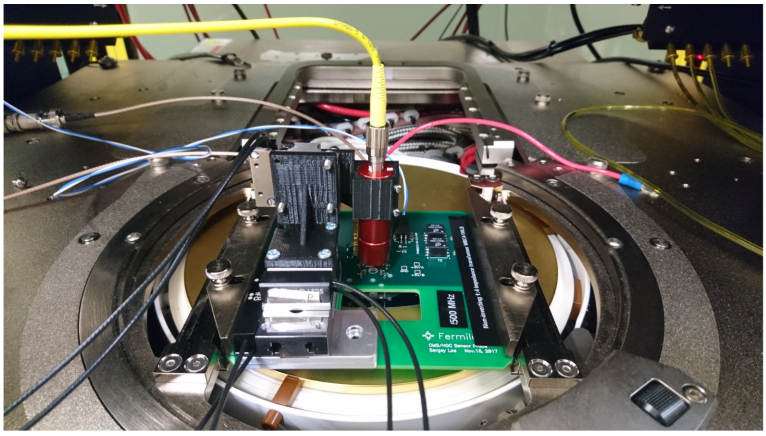

Figure 10: Detail of the probe station used for the tests of the sensors.

3.1.3 Probe Card

The probe card, shown in Figure 11, is a card that permits to make the contact between the readout circuit and the channels of the detector. The contacts are made with a mechanical system called Pogo pins. It is composed also by the readout circuit that permits to read the signal that outcomes from the detector.

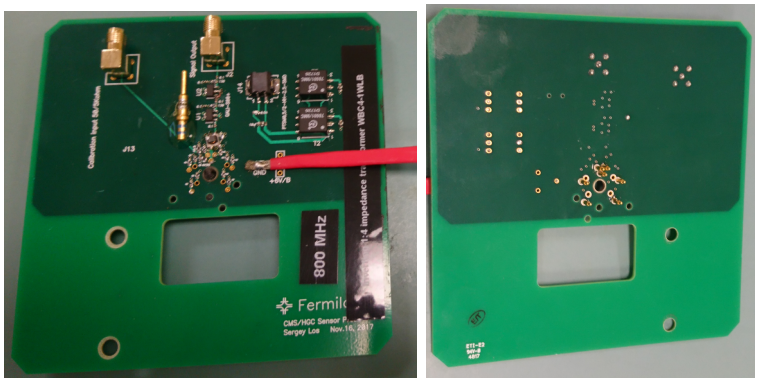

Figure 11: Probe card used for the laser test. On the left side are shown the components of the readout circuit. On the right side are shown the Pogo pins.

3.1.4 Power Supply

The power supply used for all the tests is the KEITHLEY 237, shown in Figure 12, it is used to supply the bias potential and also to measure the total current flowed through the detector. Connected to the pc it permitted via the LabVIEW software to change the bias potential during the tests.

Figure 12: KEITHLEY 237 power supply. It was also used to measure the total current flowed through the detector.

3.1.5 Oscilloscope

The signal that outcomes from the readout circuit was acquired by the oscilloscope, shown in Figure 13. The instrument made the average of 512 waveforms and the resultant waveform was processed by the LabVIEW software in order to acquire the amplitude of the signal.

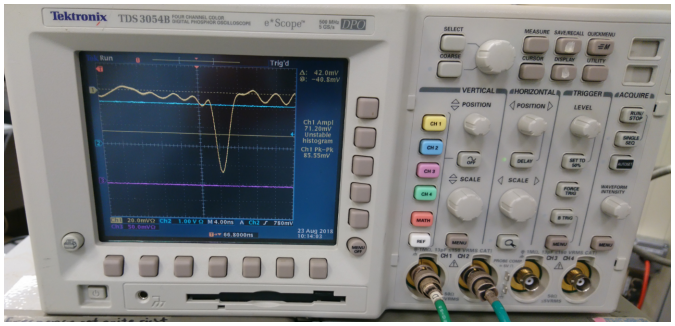

Figure 13: Oscilloscope used to acquire the waveforms in order to valuate the peak

3.2 LabVIEW Software

All the instruments used for the tests were controlled and automatized by a LabVIEW software. The algorithm moved the sensor in order to irradiate

different channels, it controlled the power supply in order to make the bias potential scans. But it also acquired the data from the oscilloscope. After the data were acquired it made the measurement of the signal amplitude, after that it saves the coordinate of the measured channel and it saves the signal amplitude. During this work I have upgraded the algorithm of the data acquisition making different preliminary studies to understand how was the more stable way to acquire the peak value of the signal. These studies showed that the use of the minimum value of the waveform was better than take the mean of the peak in a fixed time range and also than a method that make a fit of a waveform and it took the peak in an analytical way. I also made an online noise subtraction in order to increase the signal to noise ratio, in Figure 14 is shown the VI of the program that shown the waveform subtracted and the waveform of the noise.

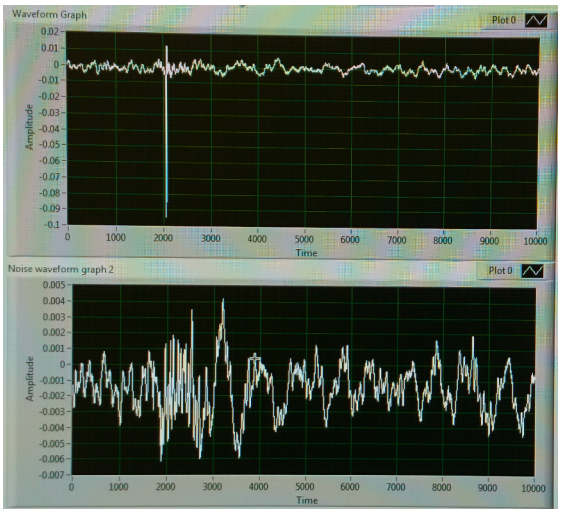

Figure 14: VI program for the noise subtraction; on the top the waveform after the noise subtraction; on the lower side the noise waveform

3.3 Results

The results of the laser test for the four Wafer are shown in Figure 15.

As you can see all the channels have a similar response to the laser. There were some problems in the contact for a few channels that can be solved just making again the contact height of the probe card and repeating

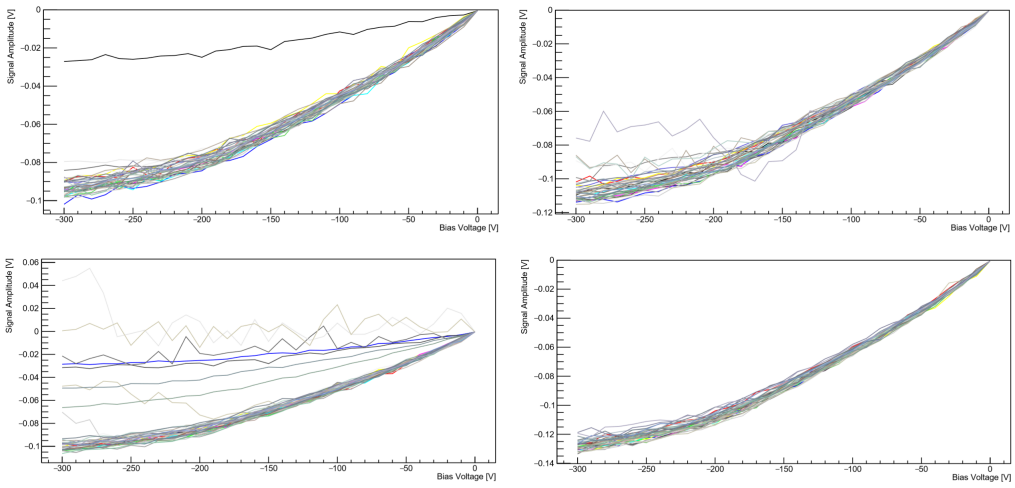

Figure 15: Signal amplitude as function of the bias potential for the channels of a Wafer. On the top starting from the left Wafer 1 and Wafer 2, on the low side Wafer 3 and Wafer 4.

the measurement. Furthermore all the Wafers have a very similar trend. The graphs also show a plateau that is not so evident as we expected. When the depletion voltage is reached the diode is fully depleted and so the charge collected should be the same even with the increasing of the bias voltage, showing an evident plateau in the pulse height graph. This problem is not well understood and some more simulation and test should be done to better understand this phenomena. A rough explanation could be that the shape of the signal that outcomes from the laser depends on the bias voltage so the peak value does not represent a correct value to estimate the total charge collected on the detector, the Figure 16 shows this issues for a single channel of the Wafer 3.

The graphs in Figure 17 shows that the channels do not have any evident pattern in terms of the signal height.

The distribution of the signal height of the channels shows that for all the wafers there is a very small spread of about $4\,mV$ at $-250\,V$ for all the wafers, Figure 18

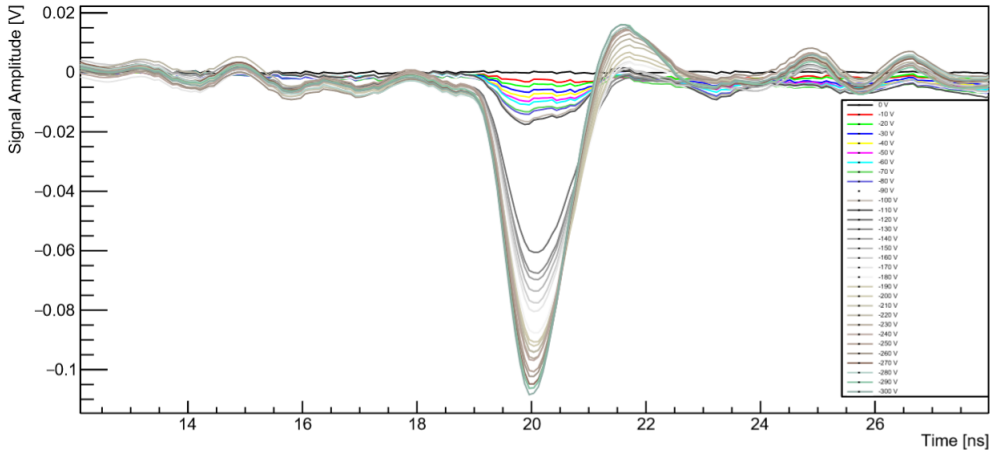

Figure 16: Signals collected at different bias voltages for a channel of the Wafer 3. The shape of the signal changes as the bias voltage increases.

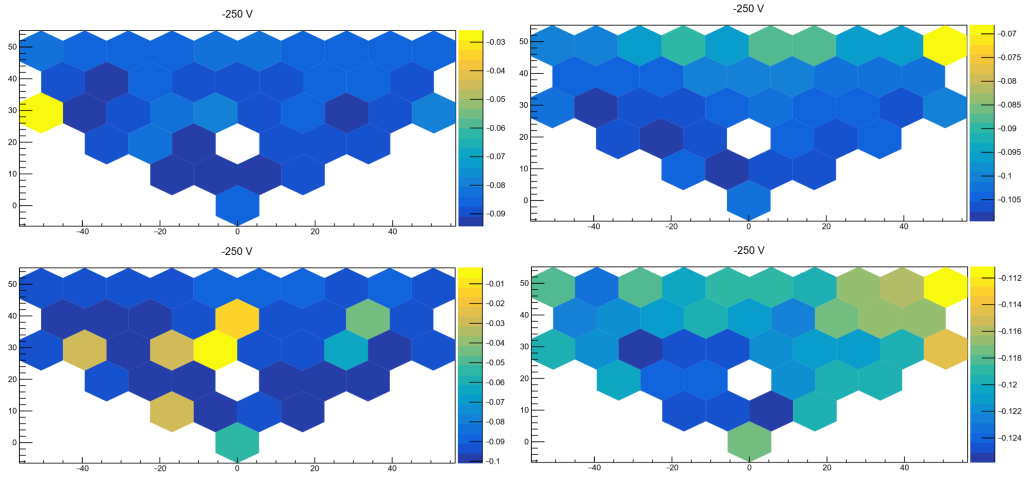

Figure 17: Map of the Signal height at a fixed bias voltage of -250 V for the channels of the Wafers.On the top starting from the left Wafer 1 and Wafer 2, on the low side Wafer 3 and Wafer 4.

4 VI Test

The VI curve of a diode permits to understand its general operation condition, and also to find the range of bias voltages out of the breakdown

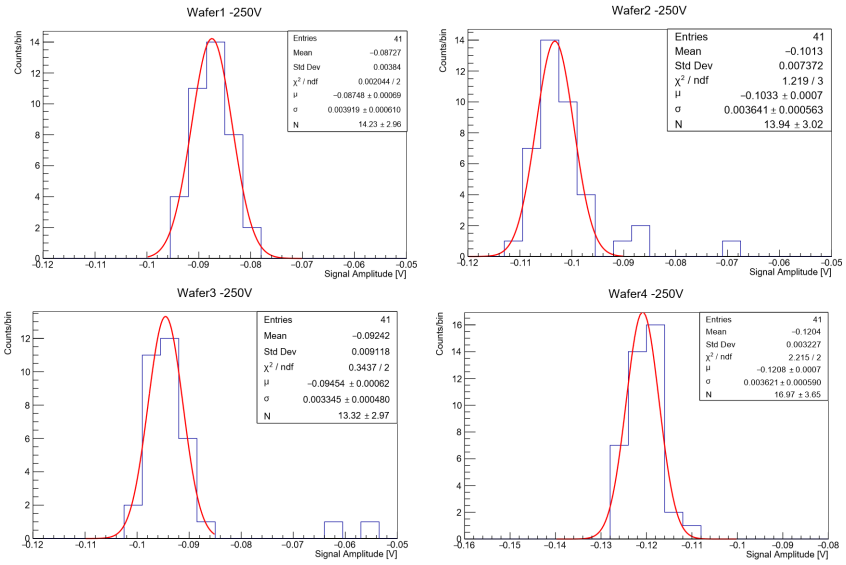

Figure 18: Signal height distribution for the channels of a Wafer at a fixed bias voltage of -250 V. On the top starting from the left Wafer 1 and Wafer 2, on the low side Wafer 3 and Wafer 4.

condition. As for the lase test, in order to better isolate the channel tested, the narrowing channels were grounded. The test consists on measuring the leakage current of the channel as a function of the bias voltages. The measurements were automatized by the automatic probe station controlled by a LabVIEW software.

4.1 Setup

The setup differs to that used for the Laser test for the use of the laser, in fact the VI curves are made in a dark condition for the detector; for the use of a picoammeter; and for a different probe card that did not contain a readout chip, but it just made the contact to the channel in order to permits the flow of the current trough the picoammeter. In Figure 19 is shown a scheme of the setup for the VI test.

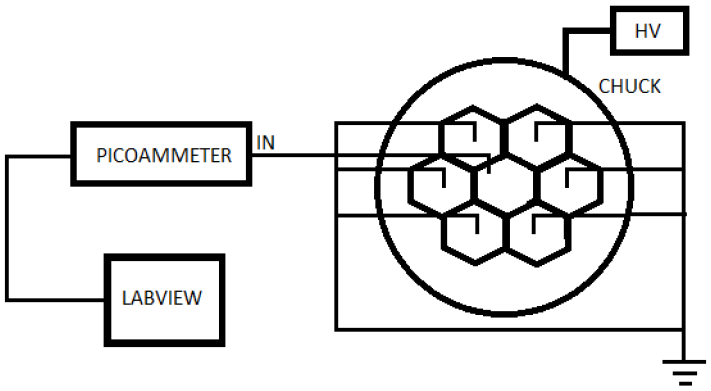

Figure 19: Scheme of the setup used for the VI test.

4.1.1 Picoammeter

The leakage current that flowed trough a single channel was measured by the Keithley 486 Picoammeter, shown in Figure 20. The instrument has a resolution of 10 fA.

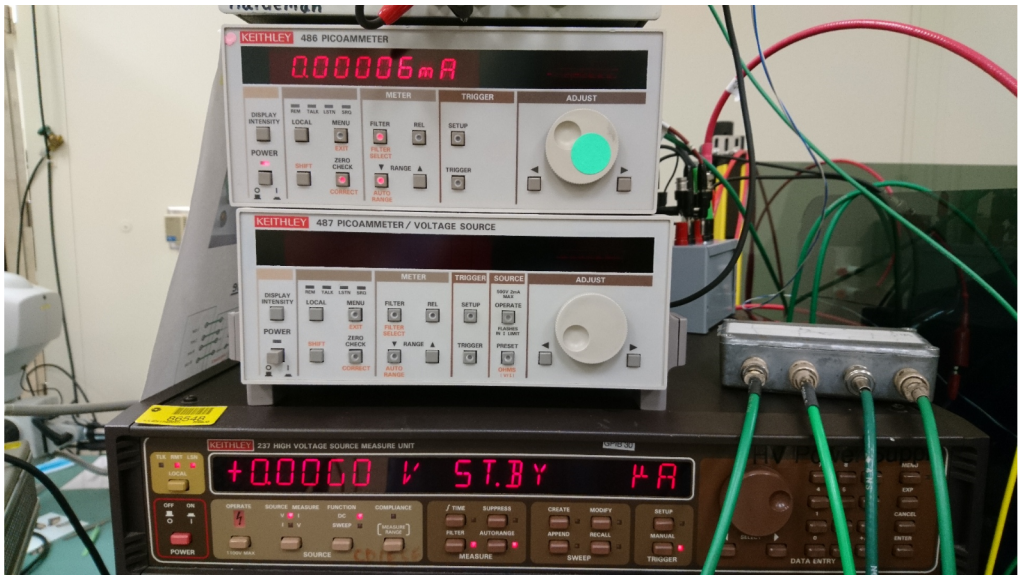

Figure 20: Keithley 486 Picoammeter. Instrument used to measure the leakage current of the detector.

4.2 Results

The VI curves, shown in Figure 21, report that Wafer 1, 3 and 4 have different trends from Wafer 2. In fact while the channels in Wafer 2 have a more regular trend and the breakdown occurs at high voltages for the channels of the other Wafers emerge a very spread out breakdown voltage that is also more low than expected. It is also evident a phenomena of saturation for the current of Wafers 1,3 and 4 that corresponds to the saturation of the total current flowing through the power supply. This suggests that the other channels were contributing to the current collected to the 7-pin setup. This effect could depend on the resistance between the six surrounding pads and the other pads of the detector. Also the resistance between channels is the only thing that differs between Wafer 2 and the others.

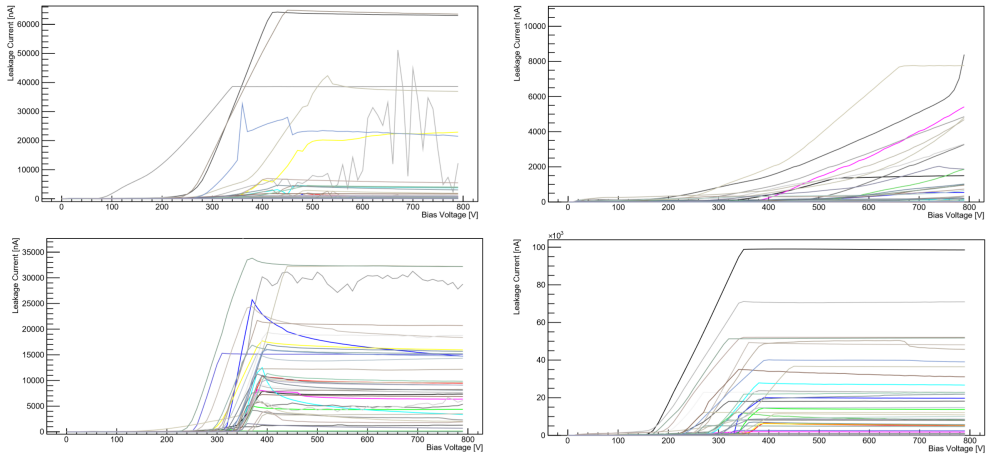

Figure 21: VI curves for the channels of the Wafers. On the top starting from the left Wafer 1 and Wafer 2, on the low side Wafer 3 and Wafer 4.

To better understand the differences between the Wafers I made another test in which I measured the potential of a single channel, so that channel was floating, as a function of the bias potential when the surroundings channels were tied to ground. The setup for this test was very similar to the VI test setup, the only difference is the use of a voltage meter instead of the picoammeter. The results of this test, shown in Figure 22, indicate that Wafer 2 has a different trend, also for the low bias voltage region. This confirm the different response between Wafers 1,3,4 and Wafer 2. This difference it may be due to a different p-stop dose in the wafers.

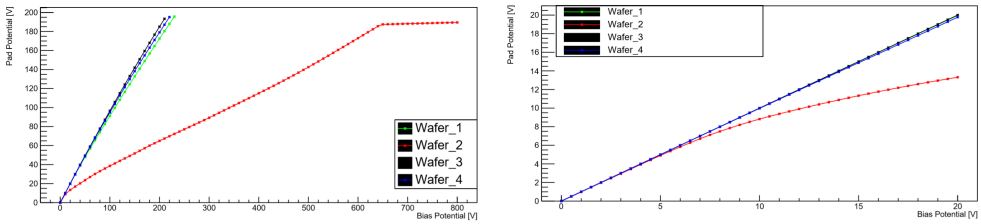

Figure 22: Voltage of a single channel of each of the four Wafers as a function of the bias voltage. On the right side a low range bias voltage test with increased step.

5 Conclusions

The test I made for the prototypes sensors for the HGCAL produced by Nhanced Semiconductor shown that there were some problems in therms of the leakage current of the channels. The differences between Wafer 2 and the others show that they could be some problems in terms of channels isolation. The charge collection efficiency was enough homogeneous between channels, all the wafers have a standard deviation of 4 mV at 250 V. But more quantitatively studies of the charge collection efficiency are needed to understand the lack of a plateau. Also studies of other wafers will allow to confirm if the differences between the wafers in the IV curve are due to the different p-stop doses. All this studies have to be repeated after the irradiation of the sensors.